Kalman Filter-based Mobile User-RIS Channel Estimation and User Localization

Zhuoxuan Ju
The George Washington University
Washington, DC
jzx0613@gwu.edu

Miloš Doroslovački
The George Washington University
Washington, DC
doroslov@gwu.edu

arXiv:2512.17112v1 [eess.SP] 18 Dec 2025

This work has been submitted to the IEEE for possible publication. Copyright may be transferred without notice, after which this version may no longer be accessible.

Abstract—In communication networks, channel estimation and user localization are challenging problems in harsh environments or signal-blocked areas. This paper introduces a novel approach to minimize the Mean Squared Error (MSE) in channel estimation between mobile users and rectangular Reconfigurable Intelligent Surfaces (RIS) within wireless communication systems. Meanwhile, the user localization is realized based on the estimated Channel State Information (CSI). In this paper, we assume a non-linear, user's position-dependent system model, for a user with high mobility, an RIS with multiple elements, and a base station (BS) with multiple antennas. After that, we apply the Kalman Filtering (KF) like algorithms to reduce MSE in estimating parameters of this time-variant channel model. Additionally, we propose a Non-Circular Noise Kalman Filter (NCNKF) to address scenarios with non-circular complex state-space noise. Furthermore, we apply the Discrete Space Fourier Transform (DSFT) method, combined with the interpolation techniques to decrease the Root Mean Squared Error (RMSE) for the user localization based on the estimated CSI. Finally, we extend the single-user case into the multi-user situation. Results show that KF can achieve lower MSE in estimating the channel than other known approaches, while the NCNKF algorithm has better performance in non-circular state-space noise scenarios. At the same time, the DSFT interpolation outperforms the other approaches with lower complexity. The study concludes with numerical comparisons and an in-depth discussion of the performance improvements enabled by our approaches.

Index Terms—Channel Estimation; User Localization; Reconfigurable Intelligent Surfaces; Non-circular Noise; Multi-user; Kalman Filtering.

I. Introduction

As Fifth-Generation (5G) technology continues to mature commercially, researchers have begun exploring the path toward future Sixth-Generation (6G) networks. Compared with previous generations, 6G is expected to meet larger performance demands, such as terabits per second (Tbps) data rates for virtual reality—which is approximately 100 times faster than 5G [1]. Nevertheless, by adopting the Terahertz (THz) Band (100 GHz–10 THz), 6G communication can achieve extremely high data rates but suffers from a very short coverage range (on the order of tens of meters) due to significant signal attenuation and absorption [2]. As a result, how to extend the communication range and maintain the signal quality is the core challenge in the next-generation network.

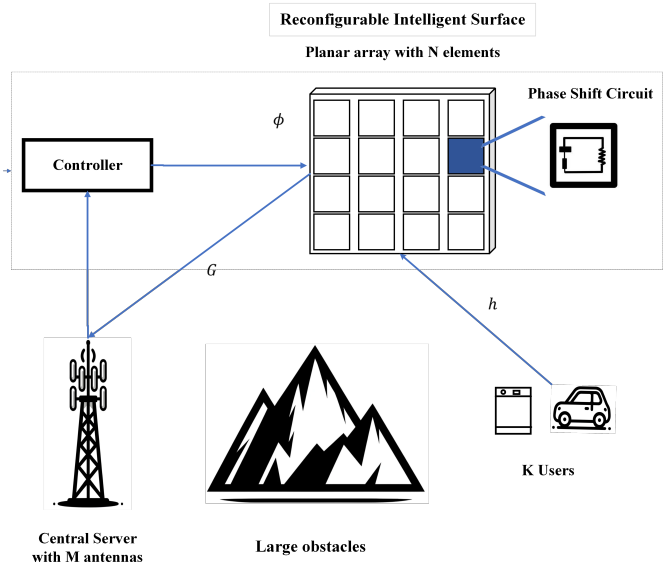

Fig. 1. The RIS-assisted Uplink Transmission Model

The Reconfigurable Intelligent Surface (RIS) [3] has recently been proposed as a promising wireless communication technology capable of altering the propagation environment in order to improve signal coverage, spectral efficiency, and energy utilization. As illustrated in Figure 1, an RIS typically consists of a planar array of programmable elements, where each element is a phase shift circuit. In most cases, the RIS is managed by a central controller, for example, a Base Station (BS). By adjusting the phase and reflection strength of each element, the RIS can focus energy toward target users or mitigate interference, thereby enhancing the signal-to-noise ratio (SNR) and achieving desired phase and amplitude control. As a result, RIS is especially advantageous in scenarios where Line-of-Sight (LoS) paths are obstructed, such as harsh environments or signal-blocked areas.

Driven by increasing performance demands, especially for coverage in blocked line-of-sight scenarios, some re-

searchers focused on improving the RIS modeling in both the physical aspect and the network aspect. From an electromagnetic standpoint, [4] proposes a physical-level model of RIS-assisted wireless communications based on local reflection coefficients and the gains of individual array elements. In [5], the authors consider optimization of a local reflection coefficient for each array element, but incorporating extensive coding schemes into network optimizers can become computationally challenging. To deal with the computation complexity, [6] derives the link-budget formulas from electromagnetic principles for anomalous reflectors, treating reflection as a collective phenomenon rather than relying on local reflection coefficients. Other works adopt different analytical perspectives. For instance, [7] employs an impedance-based analysis, focusing on voltages and currents, while [8] uses a scattering parametrization centered on incident and reflected waves.

Besides the physical modeling, recent works also concentrate on modeling the path-loss in RIS-assisted networks. A broad overview is provided in [9], covering RIS-based channel measurements, large-scale path-loss models, small-scale multipath fading models, and other key channel characterization considerations for RIS-assisted systems. Furthermore, [10] introduces a path-loss model and two surface impedance models for surface wave–assisted communications, demonstrating that the SNR can be significantly higher compared to conventional wireless setups. While path-loss modeling emphasizes large-scale attenuation over the BS–RIS–User link by augmenting traditional propagation formulas with specific parameters, scattering modeling offers a more detailed electromagnetic viewpoint. As noted in [11], scattering modeling focuses on how each RIS element individually modifies the incident wave. In addition, [12] presents an efficient method for computing the scattered electric field of RIS under multiple configurations, making it possible to model wave propagation in realistic, multipath environments.

As we mentioned before, the RIS has attracted extensive interest as a potential enabler of enhancing capacity, coverage, efficiency, and security for upcoming 6G networks. Moreover, RIS not only offers robust technical network features but also exhibits low energy consumption and hardware costs, making them highly suitable for real-world deployments. Because of these advantages, RIS can be integrated with other arising and emerging communication systems, such as mmWave communications [13], unmanned aerial vehicle (UAV) networks [14], non-orthogonal multiple access (NOMA) [15] communications, and V2X networks [16]. Meanwhile, RIS is widely used in different applications, including channel estimation (CE) [17], user localization [18], sensing and transmission [19], and security enhancement [20]. In this work, we will focus on channel estimation and user localization.

Channel estimation is fundamental for RIS-aided wireless communication systems, playing a critical role in enabling reliable transmission. Traditionally, channel estimation in single-antenna narrowband systems was handled with methods like Least Squares (LS) [21] or Minimum Mean Square Error (MMSE) [22], which rely on pilot signals embedded in transmitted waveforms. Both of these approaches have limitations. Unlike MMSE, Maximum Likelihood (ML) [23] does not require prior knowledge of the channel statistics, and it is not as sensitive to the noise as the LS estimator. However, in time-variant or high-mobility scenarios, channel estimation becomes more challenging due to the rapidly changing propagation conditions. Conventional methods often fail to capture the temporal correlation and structure of the channel. The Kalman filtering (KF) [24], renowned for its effective tracking capabilities, is extensively utilized in channel estimation, especially in scenarios involving mobile users. Meanwhile, the Extended Kalman Filter (EKF) [25] is often employed as a sub-optimal solution for the non-linear models. However, in the RIS-aided communication network, the dimensionality of the cascaded channels between the BS, RIS, and user becomes extremely high, leading to high computational complexity, especially in the multi-user cases [26]. This emphasizes the importance of continuous studying of channel estimation in RIS-aided wireless communication networks.

RIS-aided user localization [27] has emerged as a promising approach for enhancing positioning accuracy. By intelligently controlling the propagation environment, RIS can reflect signals toward desired directions, thereby improving spatial diversity and overcoming limitations caused by non-line-of-sight (NLOS) conditions. In [28], the author proposes an RIS-assisted framework to localize multiple energy-constrained devices simultaneously by exploiting propagation delay differences and optimizing the settings of both the base station and the RIS. Additionally, [29] presents a two-stage scheme that uses statistical beamforming, direction-of-arrival (DoA), and time-of-arrival (ToA) estimation to iteratively refine 3D user positions. In [30], a multi-user localization method is proposed to improve the positioning precision, but with high computation complexity. In general, how to realize user localization in high-mobility scenarios with lower computation complexity and maintaining localization accuracy is an essential challenge.

To deal with these challenges, the primary goal of this work is to develop and analyze KF-based channel estimation strategies, and DSFT-based user localization algorithms that are well aligned with real-world RIS-assisted wireless communication systems. Specifically, we aim to:

1) Establish a position-dependent, rapidly changing RIS-assisted channel model. We propose a system framework that captures the realistic mobility-

induced fluctuations in wireless channels.
2) Modify the KF for mobile channel estimation under this enhanced model. The result shows that our modified KF algorithm can achieve much better performance than the standard KF in the non-linear system model.
3) Incorporate a non-circular noise model into the KF framework and introduce a Non-Circular Noise Kalman Filtering (NCNKF) to further optimize MSE performance.
4) Adapt DSFT interpolation technique to compute the user localization based on the estimated CSI. The proposed DSFT interpolation can achieve high localization accuracy while maintaining lower computation complexity than other known approaches.
5) Extend the system model to multi-user scenarios. After using the CDMA principle, we can realize the channel estimation and user localization after reducing the users' interference.
6) Demonstrate the advantages of the proposed methods compared to existing algorithms, highlighting better adaptability and robustness in complex, time-varying environments through numerical results.

By addressing these objectives, we aim to push the application boundaries of proposed algorithms for RIS-assisted communications, ensuring that they remain both computationally tractable and robust under realistic operating conditions.

The structure of this paper is laid out as follows: Section II provides a comprehensive introduction to the system model used for representing the user's high mobility. Section III details the formulation and analysis of the KF-based algorithms for both the single and multi-user cases. The non-circular noise is introduced and the NCNKF algorithm is analyzed in Section IV. Section V proposes the DSFT interpolation method to realize user localization for both the single and multi-user cases. In Section VI, we present numerical results to demonstrate the performance and characteristics of the proposed solution. The paper concludes in Section VII, where we summarize our contributions and discuss potential future work.

II. RIS-aided Wireless Communication Framework

This section introduces a wireless communication system model incorporating RIS, featuring a position-dependent channel model and a transmission model for pilot signals sent by users. Our framework is tailored to enhance channel estimation, with improvements evaluated using MSE as the performance metric.

A. System Model

This work focuses on the uplink time-variant wireless channel, where a user seeks to connect with the base station (BS) when the connection is aided by the RIS, as shown in Fig. 1. We assume the direct channel from the BS to the user is blocked by large obstacles. The BS is equipped with M antennas, and the RIS is divided into N elements. The channel matrix between the RIS and BS, denoted by $\boldsymbol{G} \in \mathbb{C}^{M\times N}$, is assumed stationary due to the fixed positions of the BS and RIS. However, the channel vector from the user to the RIS, $\boldsymbol{h} \in \mathbb{C}^{N\times 1}$, varies over time due to user mobility. Accurate estimation of $\boldsymbol{h}$ is our primary objective, essential for improving communication reliability in this dynamic scenario.

B. Distance-based Channel Model

For analysis purposes, we divide the time into $1, 2, ..., T$ time slots. It is assumed that the channel $\boldsymbol{G}$ matrix satisfies:

$$\boldsymbol{G}_t = \boldsymbol{G}, \qquad t = 1, 2, ..., T, \tag{1}$$

where $\boldsymbol{G}$ represents a Rayleigh fading MIMO channel, where each element is a complex Gaussian variable with zero mean and same variance. Various methods, such as the on-off control method [31], have been developed to estimate the constant channel $\boldsymbol{G}$ effectively. Thus, we assume $\boldsymbol{G}$ is known and fixed, allowing us to focus on estimating the time-varying channel vector $\boldsymbol{h}_t$. The rapidly changing channel vector $\boldsymbol{h}_t$ varies as follows:

$$\boldsymbol{h}_{t+1} = \boldsymbol{h}_t + \boldsymbol{h}_t \circ \boldsymbol{v}_{t+1}, \quad t = 1, 2, ..., N-1, \tag{2}$$

where $\boldsymbol{v}_t \in \mathbb{C}^{N\times 1}$ is the process noise resulting from the user's random movement in each slot. The operator $\circ$ denotes the Hadamard product, and the initial channel vector follows $\boldsymbol{h}_1 \sim \mathcal{CN}(0, \sigma_h^2)$. The reason we consider this distance-depend channel model is explained in detail in [32]. Most existing studies on mobility [17] assume that the channel vector update is given by $\boldsymbol{h}_t = \boldsymbol{h}_{t-1} + \boldsymbol{v}_t$, neglecting the fact that channel fluctuations should depend not only on the process noise (user movement) $\boldsymbol{v}_t$ but also on the underlying channel current conditions:

$$\boldsymbol{h}_t^{(n)} = \frac{\boldsymbol{g}_t^{(n)}}{\boldsymbol{r}_t^{(n)}} e^{-j\frac{2\pi \boldsymbol{r}_t^{(n)}}{\lambda}}, \tag{3}$$

where $\boldsymbol{r}_t^{(n)}$ denotes the distance between the user and the n-th RIS element, and $\boldsymbol{g}_t^{(n)}$ represents the response of the n-th RIS element, which is considered as a constant here. $\lambda = \frac{c}{f_c}$ is the signal wavelength, where c is the speed of light and f_c is the carrier frequency. Here, let us use d to express the length of the edge of an RIS element. Based on the Fraunhofer Distance [33], the boundary distance of the near field and far field between the user and RIS d_f is defined as:

$$d_f = \frac{2(\sqrt{2}\sqrt{N}d)^2}{\lambda} = \frac{4Nd^2}{\lambda}. \tag{4}$$

To keep the far field communication scenario, we have the constraint $r_t > d_f$. The user moves $\epsilon_t = ||\vec{\epsilon}_t|| = \alpha_t \Delta t$ at t-th time slot, where α_t is the speed of the user

that follows the uniform distribution $\alpha_t \sim \mathcal{U}[0, \alpha_{\max}]$, and Δt is the duration of one time slot. Suppose the angle between $\vec{r}_{t-1}$ and $\vec{\epsilon}_t$ is μ_t. As a result, we can get the change of distance between the user and the center of RIS as:

$$\begin{aligned}\Delta r_t &= r_t - r_{t-1} = \sqrt{r_{t-1}^2 + \epsilon_t^2 - 2r_{t-1}\epsilon_t \cos\mu_t} - r_{t-1} \\ &= \sqrt{r_{t-1}^2 + \epsilon_t^2}\sqrt{1 - \frac{2r_{t-1}\epsilon_t}{r_{t-1}^2 + \epsilon_t^2}\cos\mu_t} - r_{t-1} \\ &\approx r_{t-1}\sqrt{1 - \frac{2\epsilon_t}{r_{t-1}}\cos\mu_t} - r_{t-1} \\ &\approx r_{t-1}(1 - \frac{\epsilon_t}{r_{t-1}}\cos\mu_t) - r_{t-1} \\ &= -\epsilon_t \cos\mu_t \end{aligned} \tag{5}$$

Based on the equation (3), we can represent the channel vector in the $(t+1)$-th time slot by the user's speed and moving direction with the assumption that $\frac{1}{\boldsymbol{r}_t^{(n)}} = |\boldsymbol{h}_t^{(n)}|$:

$$\begin{aligned}\boldsymbol{h}_{t+1}^{(n)} &= \frac{\boldsymbol{g}_t^{(n)}}{\boldsymbol{r}_t^{(n)} + \Delta\boldsymbol{r}_t^{(n)}} e^{-j\frac{2\pi(\boldsymbol{r}_t^{(n)} + \Delta\boldsymbol{r}_t^{(n)})}{\lambda}} \\ &= \frac{1}{1 + \frac{\Delta\boldsymbol{r}_t^{(n)}}{\boldsymbol{r}_t^{(n)}}} \frac{\boldsymbol{g}_t^{(n)}}{\boldsymbol{r}_t^{(n)}} e^{-j\frac{2\pi}{\lambda}\boldsymbol{r}_t^{(n)}} e^{-j\frac{2\pi}{\lambda}\Delta\boldsymbol{r}_t^{(n)}} \\ &= \frac{1}{1 + \Delta\boldsymbol{r}_t^{(n)}|\boldsymbol{h}_t^{(n)}|} \boldsymbol{h}_t^{(n)} e^{-j\frac{2\pi}{\lambda}\Delta\boldsymbol{r}_t^{(n)}} \\ &= \frac{e^{-j\frac{2\pi}{\lambda}\alpha_t\Delta t\cos\mu_t^{(n)}}}{1 - \alpha_t\Delta t\cos\mu_t^{(n)}|\boldsymbol{h}_t^{(n)}|} \boldsymbol{h}_t^{(n)}. \end{aligned} \tag{6}$$

C. Position-based Channel Model

Although the distance-based channel model is good enough for channel estimation, we also want to relate the CSI to the user's position, which could help us to find user localization from the CSI. Remind that d is the length of the edge of an RIS element. To establish a specific RIS model to express each channel element $h_t^{(n)}$, let us set the RIS being in the x-y plane and the center of the RIS to have the position $(0, 0)$. Then, the position of the element center of the n-th row and m-th column can be described as:

$$\begin{aligned}(x_n, y_m) =& (nd - d\frac{1+\sqrt{N}}{2}, md - d\frac{1+\sqrt{N}}{2}), \\ & n, m = 1, 2, ..., \sqrt{N}, \text{ where } \sqrt{N} \in \mathbb{Z}_+. \end{aligned} \tag{7}$$

The corresponding channel vector entry for the RIS element in positions (x, y) can be expressed as:

$$h_t(x, y) \approx \frac{1}{r_t} e^{-j\frac{2\pi}{\lambda}r_t + j\frac{2\pi}{\lambda}\cos\theta_t(x\cos\varphi_t + y\sin\varphi_t)} \tag{8}$$

where θ_t is the user elevation angle and φ_t is the user azimuth angle at the t-th time slot. For the specific position of the user at t-th time slot $\boldsymbol{p_t} = [p_{x,t}, p_{y,t}, p_{z,t}]^T$,

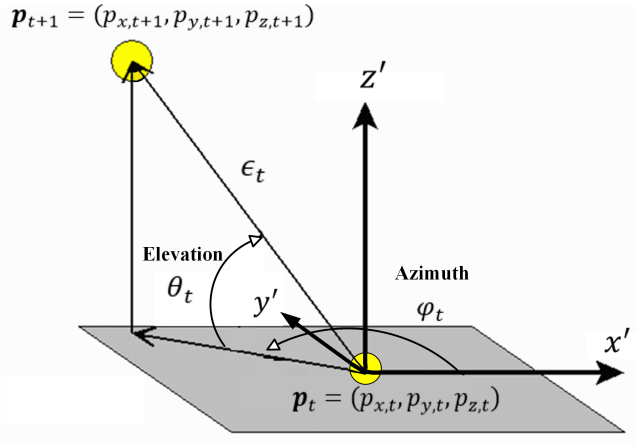

Fig. 2. The User Movement Coordinate System

the channel vector entry for the element in a given position in x-y plane can be expressed as:

$$h_t(x, y) \approx \frac{1}{r_t} e^{-j\frac{2\pi}{\lambda}r_t + j\frac{2\pi}{\lambda r_t}(xp_{x,t} + yp_{y,t})} = |h_t| e^{j\chi_t(x,y)} \tag{9}$$

where $\chi_t(x, y)$ is the phase of the channel vector only for the element at the position (x, y). As a result, for the initial distance r_0 between the user and the center of the RIS that satisfies the far field situation, the initial azimuth angle and elevation angle that follows the uniform distribution $\varphi_0 \sim \mathcal{U}[-\pi, \pi]$, $\theta_0 \sim \mathcal{U}[0, \frac{\pi}{2}]$, the corresponding initial position vector is

$$\boldsymbol{p_0} = [r_0\cos\theta_0\cos\varphi_0,\ r_0\cos\theta_0\sin\varphi_0,\ r_0\sin\theta_0]^T. \tag{10}$$

In each time slot, the user will move randomly as we mentioned in Section II-B with $\epsilon_t \sim \mathcal{U}[0, \alpha_{max}\Delta t]$, where α_{max} is the user's maximum velocity. Suppose the azimuth angle $\varphi_t \sim \mathcal{U}[-\pi, \pi]$ and the elevation angle $\theta_t \sim \mathcal{U}[-\frac{\pi}{2}, \frac{\pi}{2}]$. The corresponding user's position vector:

$$\begin{aligned}\boldsymbol{p}_{t+\Delta t} =& [p_{x,t} + \epsilon_t\cos\theta_t\cos\varphi_t, \\ & p_{y,t} + \epsilon_t\cos\theta_t\sin\varphi_t,\ p_{z,t} + \epsilon_t\sin\theta_t]^T \end{aligned} \tag{11}$$

where the user movement coordinate system is shown in the Figure 2. The distance between the user and the RIS can be calculated as:

$$r_t = \sqrt{p_{x,t}^2 + p_{y,t}^2 + p_{z,t}^2}. \tag{12}$$

With the update of the $p_{x,t}, p_{y,t}, p_{z,t}$ and r_t each time slot, we can update the channel vector between the user and different RIS elements with equation (9).

D. Signal Model

To enhance the estimation of the channel vector $\boldsymbol{h}$, the user transmits a pilot signal $s_t \in \{0, 1\}$ to the base station in each slot. Based on the previously described channel

model, the received signal at the base station, $\boldsymbol{y}_t$, is given by:

$$\begin{aligned}\boldsymbol{y}_t &= \sqrt{P_{\mathrm{tr}}}\boldsymbol{G}\mathrm{diag}(\boldsymbol{\phi}_{\mathrm{t}})\boldsymbol{h}_{\mathrm{t}}\mathrm{s}_{\mathrm{t}} + \boldsymbol{w}_{\mathrm{t}} \\ &= \boldsymbol{C}_t\boldsymbol{h}_t s_{\mathrm{t}} + \boldsymbol{w}_t, \end{aligned} \tag{13}$$

where P_{tr} denotes the transmit power. Here, $\boldsymbol{C}_t = \sqrt{P_{\mathrm{tr}}}\boldsymbol{G}\,\mathrm{diag}(\boldsymbol{\phi}_t)$ represents the equivalent channel influenced by the RIS, where $\boldsymbol{\phi}_t$ is the controllable phase shift vector of the RIS elements. The observation noise, $\boldsymbol{w}_t \in \mathbb{C}^{M\times 1}$, follows a complex normal distribution, $\boldsymbol{w}_t \sim \mathcal{CN}(0, \sigma_w^2)$. As a result, the corresponding Signal-to-Noise Ratio (SNR) can be calculated as:

$$\mathrm{SNR}_{\mathrm{t}} = \frac{1}{\mathrm{M}}\frac{||\boldsymbol{y}_{\mathrm{t}}||^2}{\sigma_{\mathrm{w}}^2} = 10\log\frac{1}{\mathrm{M}}\frac{||\boldsymbol{y}_{\mathrm{t}}||^2}{\sigma_{\mathrm{w}}^2}\ \ \mathrm{dB}. \tag{14}$$

Based on the RIS-aided communication framework we established, the system performance of the channel estimation is assessed using the Mean Squared Error (MSE) defined as:

$$\mathrm{MSE}_{\mathrm{t}} = \mathbb{E}\left[||\boldsymbol{h}_{\mathrm{t}} - \widehat{\boldsymbol{h}}_{\mathrm{t}}||^2\right], \tag{15}$$

where $\widehat{\boldsymbol{h}}_t$ is the estimated channel vector. This MSE metric quantifies the accuracy of the channel estimation by measuring the squared discrepancy between the actual and estimated channel vectors. At the same time, the used performance measure for user localization, the Normalized Root Mean Squared Error (NRMSE) is:

$$\mathrm{NRMSE}_{\mathrm{t}} = \frac{\sqrt{\mathbb{E}\left\{(p_{x,t}-\widehat{p}_{x,t})^2 + (p_{y,t}-\widehat{p}_{y,t})^2 + (p_{z,t}-\widehat{p}_{z,t})^2\right\}}}{\mathbb{E}\left\{r_t\right\}} \tag{16}$$

where $\widehat{p}_{x,t}, \widehat{p}_{y,t}, \widehat{p}_{z,t}$ are the estimated user's position for the x, y, z axis, respectively.

III. Channel Estimation based on Kalman Filtering Algorithm

In this section, we apply a modified Kalman Filter to reduce the mean squared error (MSE) in estimating parameters of our distance-dependent system model. The filter is used to track the channel vector $\boldsymbol{h}_t$ while considering variations caused by distance. We also evaluate the system's performance using the Extended Kalman Filter, which is suitable for handling the proposed non-linear system model. In addition, we discuss channel estimation in the case of multiple users.

A. Modified Kalman Filtering

Based on the system model described in Section II, we treat equation (2) as the state evolution model and equation (13) as the observation model. The observation noise $\boldsymbol{w}_t$ is assumed to follow a circularly symmetric complex Gaussian distribution. However, the term $\boldsymbol{h}_t \circ \boldsymbol{v}_t$ is only Gaussian when $\boldsymbol{h}_t$ is fixed, and $\boldsymbol{v}_t$ follows the Gaussian distribution as well. Note that under this setting, the standard Kalman Filter approach can not produce the best results, because it is only optimal when the system is linear and both the process noise and the observation noise are Gaussian.

We also assume that the reflection coefficient vectors $\boldsymbol{\phi}_i$ are persistently exciting in the N-dimensional space. This means they provide enough variation over time to allow accurate tracking of the system state. Persistent excitation helps the filter avoid drifting to incorrect values and supports stable performance. Following the approach in [17], we use orthonormal reflection coefficient vectors defined as:

$$\left[\boldsymbol{\phi}^{(0)}, ..., \boldsymbol{\phi}^{(N-1)}\right]\left[\boldsymbol{\phi}^{(0)}, ..., \boldsymbol{\phi}^{(N-1)}\right]^H = \boldsymbol{I}_N, \tag{17}$$

and $\boldsymbol{I}_N$ denotes the identity matrix of dimension $N \times N$.

The steps of the modified Kalman Filter are outlined in Algorithm 1 Description Table, highlighting the main variables used in the process. Here, $\tilde{\boldsymbol{P}}_t$ refers to the prior covariance matrix, which captures the uncertainty in the state before new data is included. $\widehat{\boldsymbol{P}}_t$ is the posterior covariance matrix, updated after incorporating the latest observations. The matrix $\boldsymbol{Q}_t$ represents the process noise covariance, scaled by a factor q and adjusted based on the estimated channel vector. The Kalman gain, $\boldsymbol{K}_t$, determines how much the filter relies on the prior estimate versus the new measurement when updating the state. $\boldsymbol{C}_t^H$ is the Hermitian transpose of the equivalent channel matrix $\boldsymbol{C}_t$, and $\widehat{\boldsymbol{h}}_{t-1}^*$ is the complex conjugate of the previous channel estimate, used to refine the current estimate. These components work together to iteratively improve the accuracy of the channel tracking, allowing for efficient updates at each time step with relatively low computational cost.

Algorithm 1 Modified Kalman Filtering

1: Initialization: $\widehat{\boldsymbol{P}}_0, q, \widehat{\boldsymbol{h}}_1, R = \sigma_w^2$
2: for each time slot t do
3: $\quad\boldsymbol{Q}_t = q\boldsymbol{I}_N\mathrm{diag}(\widehat{\boldsymbol{h}}_{\mathrm{t-1}} \circ \widehat{\boldsymbol{h}}_{\mathrm{t-1}}^*)$;
4: $\quad\tilde{\boldsymbol{P}}_t = \widehat{\boldsymbol{P}}_{t-1} + \boldsymbol{Q}_t$;
5: $\quad\boldsymbol{K}_t = \tilde{\boldsymbol{P}}_t\boldsymbol{C}_t^H(R\boldsymbol{I}_M + \boldsymbol{C}_t\tilde{\boldsymbol{P}}_t\boldsymbol{C}_t^H)^{-1}$;
6: $\quad\widehat{\boldsymbol{h}}_t = \widehat{\boldsymbol{h}}_{t-1} + \boldsymbol{K}_t(\boldsymbol{y}_t - \boldsymbol{C}_t\widehat{\boldsymbol{h}}_{t-1})$;
7: $\quad\widehat{\boldsymbol{P}}_t = (\boldsymbol{I}_N - \boldsymbol{K}_t\boldsymbol{C}_t)\tilde{\boldsymbol{P}}_t$;
8: end for

B. Multi-user Modified Kalman Filtering Channel Estimation

Code Division Multiple Access (CDMA) [34] is a spread-spectrum multiple-access technique where each user's data is multiplied by a unique pseudo-random code and transmitted over the same frequency band. At the receiver side, the signal corresponding to a specific user can be extracted by correlating the received signal with that user's code. This process helps mitigate interference and multi-path effects by spreading them across the spectrum.

Inspired by this concept, we incorporate orthogonal coding into the channel estimation process. Each user's signal is multiplied by a distinct orthogonal code, allowing their channels to be distinguished even when transmitted over the same resources. For illustration, consider a two-user scenario. Let the channel vectors of user 1 and user 2 at time slot t be denoted by $\boldsymbol{h}_{1t}, \boldsymbol{h}_{2t} \in \mathbb{C}^{N\times 1}$. The combined channel vector can be written as:

$$\boldsymbol{h}_t' = \begin{bmatrix} \boldsymbol{h}_{1t} \\ \boldsymbol{h}_{2t} \end{bmatrix} \in \mathbb{C}^{2N\times 1}. \tag{18}$$

To reduce mutual interference between the users, we assign a simple time-variant precoding vector f_t based on the time slot index:

$$f_t = \begin{cases} [1,\ 1]^T & , t \bmod 2 = 1 \quad (19a) \\ [1,-1]^T & , t \bmod 2 = 0, \quad (19b) \end{cases}$$

where the first and second entries correspond to user 1 and user 2, respectively. The received signal is then given by:

$$\boldsymbol{y}_t = f_t^T \otimes I_{M\times M} \begin{bmatrix} \boldsymbol{C}_{1t} & 0 \\ 0 & \boldsymbol{C}_{2t} \end{bmatrix} \boldsymbol{h}_t^{'} s_{\mathrm{t}} + \boldsymbol{w}_t, \tag{20}$$

where $\boldsymbol{C}_{1t}$ and $\boldsymbol{C}_{2t}$ represent the equivalent (cascaded) channel matrices for users 1 and 2, and $\boldsymbol{w}_t \in \mathbb{C}^{M\times 1}$ is the observation noise. The Kronecker product $\otimes$ with f_t alternates the user weights, enabling separations of user contributions across time slots.

Using this modified observation model, Algorithm 1 can be adapted to estimate each user's channel independently, effectively suppressing inter-user interference. This framework naturally extends to scenarios with more than two users. For $k > 2$, we assign each user a distinct code (e.g., the Discrete Fourier Transform (DFT) matrix of size k), and define a combined channel vector $\boldsymbol{h}_t' \in \mathbb{C}^{kN\times 1}$. The estimation process proceeds in a similar manner using appropriately designed precoding and observation models.

IV. Non-circular noise and NCNKF

The standard KF and EKF with an unknown time-varying process noise covariance can both yield sub-optimal estimates. Additionally, these methods assume circular complex noise, which accurately represents only a subset of realistic noise types. To address scenarios featuring non-circular complex noise, we introduce the Non-Circular Noise Kalman Filtering, designed to optimize MSE performance in the RIS-assisted setting with unknown process noise covariances.

A. Non-Circular Noise System Model

In many signal processing and wireless communication systems, noise is commonly modeled as circularly symmetric complex Gaussian (CSCG) [35], mainly because of its mathematical simplicity and the assumption that the real and imaginary components have equal covariance matrices, and screw symmetric cross-covariance matrices. However, in some practical scenarios, the noise may deviate from this ideal model and become the non-circular [36], which breaks the rotational invariance property that CSCG noise possesses. As a result, conventional estimation and filtering methods may no longer be optimal. To better utilize the statistical characteristics of non-circular noise, modified or more advanced algorithms are needed. Considering noise non-circularity can lead to noticeable improvements in estimation and detection performance, particularly in systems requiring high accuracy or operating under low signal-to-noise ratio conditions.

Before introducing the algorithm, we first define the state-space model used in the Non-Circular Noise Kalman Filter. Due to the fact that non-circular noise can introduce arbitrary correlations between the real and imaginary parts of the noise, it is necessary to treat these components separately. Starting from equation (2), we decompose the complex channel vector $\boldsymbol{h}_t$ into its real and imaginary parts, and construct a new state-space model accordingly:

$$\begin{aligned} &\boldsymbol{x}_{t+1} = \boldsymbol{x}_t + \boldsymbol{B}_t \boldsymbol{v}_{t+1}^{'} \\ &\begin{bmatrix} \mathrm{Re}\{\boldsymbol{h}_{\mathrm{t}+1}\} \\ \mathrm{Im}\{\boldsymbol{h}_{\mathrm{t}+1}\} \end{bmatrix} = \begin{bmatrix} \mathrm{Re}\{\boldsymbol{h}_{\mathrm{t}}\} \\ \mathrm{Im}\{\boldsymbol{h}_{\mathrm{t}}\} \end{bmatrix} + \\ &\begin{bmatrix} \mathrm{diag}(\mathrm{Re}\{\boldsymbol{h}_{\mathrm{t}}\}) & -\mathrm{diag}(\mathrm{Im}\{\boldsymbol{h}_{\mathrm{t}+1}\}) \\ \mathrm{diag}(\mathrm{Im}\{\boldsymbol{h}_{\mathrm{t}}\}) & \mathrm{diag}(\mathrm{Re}\{\boldsymbol{h}_{\mathrm{t}+1}\}) \end{bmatrix} \begin{bmatrix} \mathrm{Re}\{\boldsymbol{v}_{\mathrm{t}+1}\} \\ \mathrm{Im}\{\boldsymbol{v}_{\mathrm{t}+1}\} \end{bmatrix} \end{aligned} \tag{21}$$

where $\boldsymbol{x}_t = \begin{bmatrix} \mathrm{Re}\{\boldsymbol{h}_{\mathrm{t}}\} & \mathrm{Im}\{\boldsymbol{h}_{\mathrm{t}}\} \end{bmatrix}^{\mathrm{T}}$ corresponds to a $2N \times 1$ channel vector with separate real and imaginary parts, and $\boldsymbol{B}_t$ shows the relationship between the noise and channel state as:

$$\boldsymbol{B}_t = \begin{bmatrix} \mathrm{diag}(\mathrm{Re}\{\boldsymbol{h}_{\mathrm{t}}\}) & -\mathrm{diag}(\mathrm{Im}\{\boldsymbol{h}_{\mathrm{t}}\}) \\ \mathrm{diag}(\mathrm{Im}\{\boldsymbol{h}_{\mathrm{t}}\}) & \mathrm{diag}(\mathrm{Re}\{\boldsymbol{h}_{\mathrm{t}}\}) \end{bmatrix} \tag{22}$$

Next, we derive the process noise covariance in the NCNKF framework by examining how the channel vector evolves with the user's motion. This involves computing the time derivative of the channel model given in equation (3), and then multiplying it by Δt to obtain an expression for the channel variation over a short time interval:

$$\begin{aligned} \Delta \boldsymbol{h}_t^{(n)} &= \left(\frac{\Delta \boldsymbol{g}_t^{(n)}}{\boldsymbol{g}_t^{(n)}} - \frac{\Delta \boldsymbol{r}_t^{(n)}}{\boldsymbol{r}_t^{(n)}} - j\frac{2\pi}{\lambda}\Delta \boldsymbol{r}_t^{(n)}\right)\boldsymbol{h}_t^{(n)} \\ &= \left(-\frac{\Delta \boldsymbol{r}_t^{(n)}}{\boldsymbol{r}_t^{(n)}} - j\frac{2\pi}{\lambda}\Delta \boldsymbol{r}_t^{(n)}\right)\boldsymbol{h}_t^{(n)}. \end{aligned} \tag{23}$$

Here, we assume that the response of the RIS elements satisfies that $\boldsymbol{g}_t$ is a constant, which eliminates the term $\frac{\Delta \boldsymbol{g}_t^{(n)}}{\boldsymbol{g}_t^{(n)}}$ in the derivation. Based on the result in (23), we obtain the following expressions for the real and imaginary parts of the process noise component $\boldsymbol{v}_t^{(n)}$:

$$\mathrm{Re}\left\{\boldsymbol{v}_t^{(n)}\right\} = -\frac{\Delta \boldsymbol{r}_t^{(n)}}{\boldsymbol{r}_t^{(n)}}, \tag{24}$$

$$\mathrm{Im}\left\{\boldsymbol{v}_t^{(n)}\right\} = -\frac{2\pi}{\lambda}\Delta \boldsymbol{r}_t^{(n)}. \tag{25}$$

Using these expressions, we can compute the covariance matrix of the process noise in the NCNKF setting. Letting $\boldsymbol{Q}_t^{'}$ denote the covariance matrix of the augmented state vector $\boldsymbol{x}_t$, the result is:

$$\begin{aligned}\boldsymbol{Q}_t^{'} &= \mathbb{E}\left\{\begin{bmatrix}\mathrm{Re}\{\boldsymbol{v}_\mathrm{t}\}\\ \mathrm{Im}\{\boldsymbol{v}_\mathrm{t}\}\end{bmatrix}\begin{bmatrix}\mathrm{Re}\{\boldsymbol{v}_\mathrm{t}^\mathrm{T}\} & \mathrm{Im}\{\boldsymbol{v}_\mathrm{t}^\mathrm{T}\}\end{bmatrix}\right\}\\ &= \mathbb{E}\left\{\begin{bmatrix}\mathrm{Re}\{\boldsymbol{v}_\mathrm{t}\}\mathrm{Re}\{\boldsymbol{v}_\mathrm{t}^\mathrm{T}\} & \mathrm{Re}\{\boldsymbol{v}_\mathrm{t}\}\mathrm{Im}\{\boldsymbol{v}_\mathrm{t}^\mathrm{T}\}\\ \mathrm{Im}\{\boldsymbol{v}_\mathrm{t}\}\mathrm{Re}\{\boldsymbol{v}_\mathrm{t}^\mathrm{T}\} & \mathrm{Im}\{\boldsymbol{v}_\mathrm{t}\}\mathrm{Im}\{\boldsymbol{v}_\mathrm{t}^\mathrm{T}\}\end{bmatrix}\right\}\\ &\approx \begin{bmatrix}\mathbb{E}\left\{\frac{\Delta r_t^2}{r_t^2}\right\}\mathbb{1}\mathbb{1}^T & \frac{2\pi}{\lambda}\mathbb{E}\left\{\frac{\Delta r_t^2}{r_t}\right\}\mathbb{1}\mathbb{1}^T\\ \frac{2\pi}{\lambda}\mathbb{E}\left\{\frac{\Delta r_t^2}{r_t}\right\}\mathbb{1}\mathbb{1}^T & \frac{4\pi^2}{\lambda^2}\mathbb{E}\left\{\Delta r_t^2\right\}\mathbb{1}\mathbb{1}^T\end{bmatrix}\\ &\approx \begin{bmatrix}\mathbb{E}\left\{\Delta r_t^2\right\}|h_t|^2\mathbb{1}\mathbb{1}^T & \frac{2\pi}{\lambda}\mathbb{E}\left\{\Delta r_t^2\right\}|h_t|\mathbb{1}\mathbb{1}^T\\ \frac{2\pi}{\lambda}\mathbb{E}\left\{\Delta r_t^2\right\}|h_t|\mathbb{1}\mathbb{1}^T & \frac{4\pi^2}{\lambda^2}\mathbb{E}\left\{\Delta r_t^2\right\}\mathbb{1}\mathbb{1}^T\end{bmatrix}\end{aligned} \tag{26}$$

where $\mathbb{1}$ is a $N\times 1$ vector with all the elements equal to 1, $|\boldsymbol{h}_t|$ is the point-wise absolute value of the channel vector $\boldsymbol{h}_t$. Under the far-field condition, we assume $\frac{1}{\boldsymbol{r}_t^{(n)}} = |\boldsymbol{h}_t^{(n)}| \approx r_0^{-1}$, where r_0 is the distance from the user to the center of the RIS, and $n\in[1,N]$. Based on the user's movement model that we introduced in Section II-B, we can find the $\mathbb{E}\left\{(\Delta r_t)^2\right\}$ from (5) as:

$$\begin{aligned}\mathbb{E}\left\{(\Delta r_t)^2\right\} &= \mathbb{E}\left\{(\epsilon_t^2\cos^2\mu_t\right\} = \mathbb{E}\left\{\alpha_t^2(\Delta t)^2\cos^2\mu_t\right\}\\ &= \frac{1}{2}\mathbb{E}\left\{\alpha_t^2\right\}(\Delta t)^2\\ &= \frac{1}{6}\alpha_{\max}^2(\Delta t)^2\end{aligned} \tag{27}$$

where $\mathbb{E}\left\{(\alpha_t)^2\right\} = \frac{1}{3}\alpha_{\max}^2$ is because of assumption that the user's speed α_t follows the uniform distribution $\alpha_t \sim \mathcal{U}[0,\alpha_{\max}]$. The corresponding process noise covariance matrix, adjusted based on the channel vector, is given by:

$$\boldsymbol{Q}_t = \boldsymbol{B}_t\boldsymbol{Q}_t'\boldsymbol{B}_t^T, \tag{28}$$

and this matrix will be used in the NCNKF algorithm to model channel dynamics more accurately by replacing the $\boldsymbol{h}_t$ by $\widehat{\boldsymbol{h}}_t$.

Based on the state-space model defined in (21), we now revise the observation model (13) in the NCNKF framework as:

$$\begin{aligned}\boldsymbol{y}_t^{'} &= \boldsymbol{C}_t^{'}\boldsymbol{x}_t s_t + \boldsymbol{w}_t^{'}\\ \begin{bmatrix}\mathrm{Re}\{\boldsymbol{y}_\mathrm{t}\}\\ \mathrm{Im}\{\boldsymbol{y}_\mathrm{t}\}\end{bmatrix} &= \begin{bmatrix}\mathrm{Re}\{\boldsymbol{C}_\mathrm{t}\} & -\mathrm{Im}\{\boldsymbol{C}_\mathrm{t}\}\\ \mathrm{Im}\{\boldsymbol{C}_\mathrm{t}\} & \mathrm{Re}\{\boldsymbol{C}_\mathrm{t}\}\end{bmatrix}\begin{bmatrix}\mathrm{Re}\{\boldsymbol{h}_\mathrm{t}\}\\ \mathrm{Im}\{\boldsymbol{h}_\mathrm{t}\}\end{bmatrix}s_t\\ &\quad + \begin{bmatrix}\mathrm{Re}\{\boldsymbol{w}_\mathrm{t}\}\\ \mathrm{Im}\{\boldsymbol{w}_\mathrm{t}\}\end{bmatrix}\end{aligned} \tag{29}$$

where $\boldsymbol{y}_t^{'} \in \mathbb{C}^{2N\times 1}$ represents the separated real and imaginary parts of the received signal. Similarly, $\boldsymbol{C}_t^{'}$ and $\boldsymbol{w}_t^{'}$ represent the separated real and imaginary parts of the cascaded channel and observation noise, respectively. Assume that the real part and the imaginary part in the observation noise are independent and identically distributed, the observation noise covariance matrix $\boldsymbol{R}$ can be calculated as:

$$\begin{aligned}\boldsymbol{R} &= \mathbb{E}\left\{\boldsymbol{w}_t\boldsymbol{w}_t^T\right\}\\ &= \mathbb{E}\left\{\begin{bmatrix}\mathrm{Re}\{\boldsymbol{w}_\mathrm{t}\}\mathrm{Re}\{\boldsymbol{w}_\mathrm{t}^\mathrm{T}\} & \mathrm{Re}\{\boldsymbol{w}_\mathrm{t}\}\mathrm{Im}\{\boldsymbol{w}_\mathrm{t}^\mathrm{T}\}\\ \mathrm{Im}\{\boldsymbol{w}_\mathrm{t}\}\mathrm{Re}\{\boldsymbol{w}_\mathrm{t}^\mathrm{T}\} & \mathrm{Im}\{\boldsymbol{w}_\mathrm{t}\}\mathrm{Im}\{\boldsymbol{w}_\mathrm{t}^\mathrm{T}\}\end{bmatrix}\right\}\\ &= \begin{bmatrix}\frac{\sigma_w^2}{2} & \cdots & 0\\ \vdots & \ddots & \vdots\\ 0 & \cdots & \frac{\sigma_w^2}{2}\end{bmatrix}\end{aligned} \tag{30}$$

B. Non-Circular Noise Kalman Filtering Algorithm

Algorithm 2 Non-Circular Noise Kalman Filtering

1: Initialization: $\widehat{\boldsymbol{P}}_0, \widehat{\boldsymbol{x}}_1, \boldsymbol{R} = \frac{\sigma_w^2}{2}\boldsymbol{I}_{2M}$
2: for each time slot t do
3: Update $\boldsymbol{B}_t$ based on (22);
4: Update $\boldsymbol{Q}_t^{'}$ based on (26);
5: $\boldsymbol{Q}_t = \boldsymbol{B}_t\boldsymbol{Q}_t^{'}\boldsymbol{B}_t^T$;
6: $\tilde{\boldsymbol{P}}_t = \widehat{\boldsymbol{P}}_{t-1} + \boldsymbol{Q}_t$;
7: $\boldsymbol{K}_t = \tilde{\boldsymbol{P}}_t\boldsymbol{C}_t^{'T}(\boldsymbol{R} + \boldsymbol{C}_t^{'}\tilde{\boldsymbol{P}}_t\boldsymbol{C}_t^{'T})^{-1}$;
8: $\widehat{\boldsymbol{x}}_t = \widehat{\boldsymbol{x}}_{t-1} + \boldsymbol{K}_t(\boldsymbol{y}_t^{'} - \boldsymbol{C}_t^{'}\widehat{\boldsymbol{x}}_{t-1})$;
9: $\widehat{\boldsymbol{h}}_t^{(n)} = \widehat{\boldsymbol{x}}_{\boldsymbol{t}}{}^{(n)} + j\widehat{\boldsymbol{x}}_{\boldsymbol{t}}{}^{(n+N)}, \quad n = 1,2,...,N$;
10: $\widehat{\boldsymbol{P}}_t = (\boldsymbol{I}_{2N} - \boldsymbol{K}_t\boldsymbol{C}_t^{'})\tilde{\boldsymbol{P}}_t$;
11: end for

Based on the system model and the associated covariance matrices described earlier, the main steps of the NCNKF algorithm are summarized in Algorithm 2 Description Table. In this formulation, $\widehat{\boldsymbol{h}}_t^{(n)}$ represents the n-th element of the estimated channel vector $\widehat{\boldsymbol{h}}_t$ for $n\in[1,N]$. The relationship $\widehat{\boldsymbol{h}}_t^{(n)} = \widehat{\boldsymbol{x}}_{\boldsymbol{t}}{}^{(n)} + j\widehat{\boldsymbol{x}}_{\boldsymbol{t}}{}^{(n+N)}$ shows how the real-valued state vector $\boldsymbol{x}_t$ is mapped back to the complex-valued channel vector by combining its real and imaginary parts at each time step. This reconstruction is necessary for computing the squared error between the estimated and actual channel vectors, which is used to evaluate the performance of the NCNKF algorithm. In this manner, channel estimation can be realized even if the users do not move as we introduced before, as long as we know the variance of the user velocity and direction to calculate (27).

C. Channel Estimation Rate

We notice that in most of the existing work, the duration of each time slot will be given directly but without any optimization. However, the time interval Δt is a very important parameter to control the processing frequency of the KF. In other words, a larger value of Δt may worsen KF performance due to large updates of the channel vector caused by the user's movement. In contrast, a smaller value of Δt will lead to a lack of time for both pilot transmission and data transmission, especially in MIMO cases. As a result, it is important to decide appropriate values of the KF algorithm processing

frequency in our proposed system models to achieve good performance.

Consider the system model proposed in Section II-B. We can take the absolute value of (23) on both side to get:

$$|\Delta \boldsymbol{h}_t^{(n)}| = |\boldsymbol{h}_t^{(n)}| \sqrt{\frac{[\Delta \boldsymbol{r}_t^{(n)}]^2}{[\boldsymbol{r}_t^{(n)}]^2} + \frac{4\pi^2}{\lambda^2}[\Delta \boldsymbol{r}_t^{(n)}]^2}. \tag{31}$$

Squaring of both sides of (31) gives:

$$|\Delta \boldsymbol{h}_t^{(n)}|^2 = \left(\frac{[\Delta \boldsymbol{r}_t^{(n)}]^2}{[\boldsymbol{r}_t^{(n)}]^2} + \frac{4\pi^2}{\lambda^2}[\Delta \boldsymbol{r}_t^{(n)}]^2 \right) |\boldsymbol{h}_t^{(n)}|^2. \tag{32}$$

By taking the expectation on both sides of (32) we get:

$$\begin{aligned} &\mathbb{E}\left\{ |\Delta \boldsymbol{h}_t^{(n)}|^2 \right\} \\ &= \mathbb{E}\left\{ \left(\frac{1}{[r_t^{(n)}]^2} + \frac{4\pi^2}{\lambda^2} \right) |\boldsymbol{h}_t^{(n)}|^2 \right\} \mathbb{E}\left\{ [\Delta \boldsymbol{r}_t^{(n)}]^2 \right\} \\ &\approx \frac{4\pi^2}{\lambda^2} \mathbb{E}\left\{ |\boldsymbol{h}_t^{(n)}|^2 \right\} \mathbb{E}\left\{ [\Delta \boldsymbol{r}_t^{(n)}]^2 \right\} \end{aligned} \tag{33}$$

since $\Delta \boldsymbol{r}_t^{(n)}$ is assumed independent of $\boldsymbol{r}_t^{(n)}$, and $\approx$ holds since $\frac{1}{[r_t^{(n)}]^2}$ is much smaller than $\frac{4\pi^2}{\lambda^2}$ due to the assumption of the far field scenario. By dividing with $\mathbb{E}\left\{ |\boldsymbol{h}_t^{(n)}|^2 \right\}$ the both side of (33) we get:

$$\frac{\mathbb{E}\left\{ |\Delta \boldsymbol{h}_t^{(n)}|^2 \right\}}{\mathbb{E}\left\{ |\boldsymbol{h}_t^{(n)}|^2 \right\}} = \frac{2\pi^2}{3\lambda^2} \alpha_{max}^2 \Delta t^2 \leq \gamma \tag{34}$$

where the left side of (34) expresses how much the channel vector changes in the t-th time slot. The normalized expectation of the norm squared of $\Delta \boldsymbol{h}$ is assumed smaller than γ, where γ is a threshold of the norm change of CSI per time slot. As a result, we can specify the range of the Δt as:

$$\frac{1}{B} \leq \Delta t \leq \frac{\sqrt{6\gamma}\lambda}{2\pi \alpha_{max}} \tag{35}$$

where B is the bandwidth in the system. In our system model, we assume that the channel is almost constant during one time slot, which is known as the coherence time as well. [37] considers that this time difference should not be set to let the channel correlation coefficient fall below 0.9, which indicates that γ should be set less than 0.1. In this manner, we can adjust the appropriate channel estimation rate according to the user's velocity.

V. User Localization

CSI is an essential measurement in wireless communication networks. In Section III, we list three different algorithms to realize channel estimation, which can help us to enhance the transmission quality and improve the system efficiency. In addition, because the channel is generated based on the user's position, it is possible to extract the user's real-time localization information based on the CSI we obtained before. In this section, we will use the DSFT interpolation method to realize the user localization.

A. DSFT method

The Discrete Space Fourier Transform converts discrete-space signals into their continuous frequency representation, enabling spectral analysis for signal processing. Here we consider the DSFT method, which only has the constraint that $d \leq \frac{\lambda}{2}$ [38]. Based on the position-based channel model that we generated in (8), we can formulate the 2-D DSFT of the channel matrix as:

$$\begin{aligned} &H_t(a,b) \\ &= \sum_{n=1}^{\sqrt{N}} \sum_{m=1}^{\sqrt{N}} \frac{1}{r_t} e^{-j\frac{2\pi}{\lambda} r_t + j\frac{2\pi}{\lambda r_t}(x_n p_{x,t} + y_m p_{y,t})} e^{-jan} e^{-jbm} \\ &= \frac{1}{r_t} e^{-j\frac{2\pi}{\lambda} r_t} e^{-j\frac{2\pi}{\lambda}(1+\sqrt{N})d(\frac{p_{x,t}}{r_t} + \frac{p_{y,t}}{r_t})} \\ &e^{-j\frac{1+\sqrt{N}}{2}(a - \frac{2\pi}{\lambda}\frac{p_x}{r_t}d)} \frac{\sin(\frac{\sqrt{N}}{2}(a - \frac{2\pi}{\lambda}\frac{p_x}{r_t}d))}{\sin(\frac{1}{2}(a - \frac{2\pi}{\lambda}\frac{p_x}{r_t}d))} \\ &e^{-j\frac{1+\sqrt{N}}{2}(b - \frac{2\pi}{\lambda}\frac{p_y}{r_t}d)} \frac{\sin(\frac{\sqrt{N}}{2}(b - \frac{2\pi}{\lambda}\frac{p_y}{r_t}d))}{\sin(\frac{1}{2}(b - \frac{2\pi}{\lambda}\frac{p_y}{r_t}d))}. \end{aligned} \tag{36}$$

Here, a and b denote the spatial frequency variables along the x and y-axes, respectively, characterizing the channel response in the spatial frequency domain in DSFT. As a result, the absolute value of the 2D-DSFT can be obtained by:

$$\begin{aligned} &|H_t(a,b)| = \\ &\frac{1}{r_t} \left| \frac{\sin(\frac{\sqrt{N}}{2}(a - \frac{2\pi}{\lambda}\frac{p_x}{r_t}d))}{\sin(\frac{1}{2}(a - \frac{2\pi}{\lambda}\frac{p_x}{r_t}d))} \frac{\sin(\frac{\sqrt{N}}{2}(b - \frac{2\pi}{\lambda}\frac{p_y}{r_t}d))}{\sin(\frac{1}{2}(b - \frac{2\pi}{\lambda}\frac{p_y}{r_t}d))} \right|. \end{aligned} \tag{37}$$

We can find the corresponding (a_0, b_0) as the argmax of the absolute value of the 2D-DSFT. Suppose that (k_0, l_0) is the row and column of the largest element in the 2D- Discrete Fourier Transform (DFT) that is used to calculate 2D-DSFT on the discrete frequency grid $(\frac{2\pi k}{N_{DFT}}, \frac{2\pi l}{N_{DFT}})$, where N_{DFT} is the size of the DFT in one dimension, and $k, l \in \{0, N_{DFT} - 1\}$. Then $(\widehat{a}_0, \widehat{b}_0)$ estimates the (a_0, b_0) as:

$$\widehat{a}_0 = \begin{cases} \frac{2\pi}{N_{DFT}} k_0 & , k_0 < \frac{N_{DFT}}{2} \quad (38a) \\ \frac{2\pi}{N_{DFT}} (k_0 - N_{DFT}) & , \text{otherwise} \quad (38b) \end{cases}$$

$$\widehat{b}_0 = \begin{cases} \frac{2\pi}{N_{DFT}} l_0 & , k_0 < \frac{N_{DFT}}{2} \quad (39a) \\ \frac{2\pi}{N_{DFT}} (l_0 - N_{DFT}) & , \text{otherwise.} \quad (39b) \end{cases}$$

At the same time, theoretically, the value of the (a_0, b_0) should follow the relationship based on (37):

$$a_0 = \frac{2\pi d}{\lambda}\frac{p_{x,t}}{r_t}, \tag{40}$$

$$b_0 = \frac{2\pi d}{\lambda}\frac{p_{y,t}}{r_t}, \tag{41}$$

which helps us to find the estimated position of the user:

$$\widehat{p}_{x,t} = \widehat{a}_0\frac{\lambda}{2\pi d}r_t, \tag{42}$$

$$\widehat{p}_{y,t} = \widehat{b}_0\frac{\lambda}{2\pi d}r_t, \tag{43}$$

Based on the estimated $\widehat{p}_{x,t}, \widehat{p}_{y,t}$ and $\widehat{h}_t$, we can update the $\widehat{p}_{z,t}$ with the following equations:

$$\widehat{p}_{z,t} = \sqrt{\frac{1}{|\widehat{h}_t|^2} - \widehat{p}_{x,t}^2 - \widehat{p}_{y,t}^2}. \tag{44}$$

After updating the position of the user for all three directions, we can calculate the error of the localization S_t as:

$$S_t = \sqrt{(p_{x,t} - \widehat{p}_{x,t})^2 + (p_{y,t} - \widehat{p}_{y,t})^2 + (p_{z,t} - \widehat{p}_{z,t})^2} \tag{45}$$

and the corresponding normalized root mean squared errors (NRMSE) w.r.t. the distance between the user and RIS are defined as:

$$\begin{aligned}\mathrm{NRMSE_t} &= \frac{\mathrm{RMSE_t}}{\mathbb{E}\{\mathrm{r_t}\}} \\ &= \frac{\sqrt{\mathbb{E}\{(p_{x,t} - \widehat{p}_{x,t})^2 + (p_{y,t} - \widehat{p}_{y,t})^2 + (p_{z,t} - \widehat{p}_{z,t})^2\}}}{\mathbb{E}\{\mathrm{r_t}\}}.\end{aligned} \tag{46}$$

B. DSFT Interpolation Method

Although the performance of the DSFT method can be improved as we increase the number of elements or the DFT resolution, some other challenges appear at the same time. The main problem is that the DFT resolution is not in general high enough to reach the exact global maximum of $H_t(a, b)$, so we have to keep increasing the resolution to make the sampled DSFT point closer to the global maximum, which increases the computation complexity dramatically.

As a result, to avoid using higher DFT resolution, we will use the interpolation method, which is based on the position of the maximum of a parabola defined by the DFT value at the point $k_o(l_0)$ and its two neighbors. Based on the relationships between $H_t(a, b)$ and the DFT $H_t^{'}(k, l)$, for the absolute value of the 2D-DSFT we can write:

$$|H_t(a, b)|\Big|_{a=\frac{2\pi}{N_{DFT}}k,\ b=\frac{2\pi}{N_{DFT}}} = |H_t^{'}(k, l)|. \tag{47}$$

Remind that (k_0, l_0) specifies the row and column of the largest element in the 2D-DFT, so the position of global maximum obtained by parabola interpolation based on $k_0 - 1,\ k_0,\ k_0 + 1$, (i.e, $l_0 - 1,\ l_0,\ l_0 + 1$) is

$$\begin{aligned}k_0^\star =& \frac{1}{2}\frac{|H_t(k_0 - 1, l_0)| - |H_t(k_0 + 1, l_0)|}{|H_t(k_0 - 1, l_0)| - 2|H_t(k_0, l_0)| + |H_t(k_0 + 1, l_0)|} \\ &+ k_0\end{aligned} \tag{48}$$

$$\begin{aligned}l_0^\star =& \frac{1}{2}\frac{|H_t(k_0, l_0 - 1)| - |H_t(k_0, l_0 + 1)|}{|H_t(k_0, l_0 - 1)| - 2|H_t(k_0, l_0)| + |H_t(k_0, l_0 + 1)|} \\ &+ l_0.\end{aligned} \tag{49}$$

Based on the point $(k_0^\star, l_0^\star)$, we can estimate $(\widehat{a}_0^\star, \widehat{b}_0^\star)$:

$$\widehat{a}_0^\star = \begin{cases} \frac{2\pi}{N_{DFT}}k_0^\star & \text{, if } k_{0i} < \frac{N_{DFT}}{2}, \\ \frac{2\pi}{N_{DFT}}(k_0^\star - N_{DFT}) & \text{, otherwise,} \end{cases} \tag{50}$$

$$\widehat{b}_0^\star = \begin{cases} \frac{2\pi}{N_{DFT}}l_0^\star & \text{, if } k_{0i} < \frac{N_{DFT}}{2}, \\ \frac{2\pi}{N_{DFT}}(l_0^\star - N_{DFT}) & \text{, otherwise,} \end{cases} \tag{51}$$

We can use similar steps as described in the last section to estimate the user's position, which is summarized in the Algorithm 3 Description Table.

Algorithm 3 User Localization Based on DSFT Interpolation

1: Input: $\widehat{\boldsymbol{h}}_t$ obtained from Algorithm 1 or 2
2: for each time slot t do
3: Using 2-D DFT on the estimated channel $\widehat{\boldsymbol{h}}_t$ with 1-D size N_{DFT};
4: Find the row and column (k_0, l_0) of the largest element in the 2-D DFT matrix;
5: Use the interpolation to update $(k_0^\star, l_0^\star)$ from (k_0, l_0) with (48) and (49);
6: Calculate $(\widehat{a}_0^\star, \widehat{b}_0^\star)$ from (50) and (51);
7: Update user's position $(\widehat{p}_{x,t}, \widehat{p}_{y,t}, \widehat{p}_{z,t})$ based on (42), (43) and (44);
8: Calculate the error of localization $S_t = \sqrt{(p_{x,t} - \widehat{p}_{x,t})^2 + (p_{y,t} - \widehat{p}_{y,t})^2 + (p_{z,t} - \widehat{p}_{z,t})^2}$;
9: end for

C. Multi-user localization

Accurate localization of multiple users is a fundamental problem in wireless communication systems, particularly in scenarios involving shared spectrum and limited resources. The main challenge arises from inter-user interference, which can significantly degrade the accuracy of both channel estimation and position inference.

To address this issue, we leverage the precoding strategy described in Section III-B, which extends naturally to the multi-user setting. The overall process for multi-user channel estimation and user localization is summarized in Algorithm 4. In this formulation, $\boldsymbol{h}_{it}$ represents the i-th user's channel vector at time slot t, and $\boldsymbol{C}_{it}$ denotes the corresponding cascaded channel matrix incorporating the RIS and BS response. The estimated position of user

i at time t is denoted by $(\widehat{p}_{x,t}^{(i)}, \widehat{p}_{y,t}^{(i)}, \widehat{p}_{z,t}^{(i)})$. The algorithm first constructs the combined observation model using the coding matrix, applies one of the previously introduced filtering methods (Algorithm 1 or 2) to obtain the estimated multi-user CSI, and finally performs localization for each user based on their estimated channel.

Algorithm 4 Multi-user Channel Estimation and User Localization

1: Input: Number of RIS element N, number of BS antennas M, number of users k;
2: Design the orthonormal matrix f_t based on the users number k;
3: $\boldsymbol{h}_t = [\boldsymbol{h}_{1t}^T, \boldsymbol{h}_{2t}^T, ..., \boldsymbol{h}_{kt}^T]^T$;
4: $\boldsymbol{C}_t = f_t^T \otimes I_{M\times M}\text{diag}(\boldsymbol{C}_{1t}, \boldsymbol{C}_{2t}, ..., \boldsymbol{C}_{kt})$;
5: $\boldsymbol{y}_t = \boldsymbol{C}_t \boldsymbol{h}_t s_t + \boldsymbol{w}_t$,;
6: Obtained $\widehat{\boldsymbol{h}}_t$ from Algorithm 1 or 2;
7: $\widehat{\boldsymbol{h}}_{it} = \widehat{\boldsymbol{h}}_t((i-1)N+1 : iN), \qquad i = 1, 2, ..., k$;
8: Update i-th user's position $(\widehat{p}_{x,t}^{(i)}, \widehat{p}_{y,t}^{(i)}, \widehat{p}_{z,t}^{(i)})$ from Algorithm 3;

VI. Numerical Result

We begin by presenting simulation results illustratory the influence of key parameters on KF-based algorithms and comparing the performance of KF-based algorithms for channel estimation. Subsequently, we compare various algorithms for user localization based on the estimated CSI. Additionally, we explore other parameters that significantly impact the performance of these algorithms. Finally, we consider the multi-user scenario to assess the effectiveness of Algorithm 4. Unless otherwise specified, the experiment settings adhere to the parameters specified in Table I. We will employ the MSE metric to evaluate the performance of channel estimation, while the normalized RMSE metric will be used to assess the performance of user localization.

A. Single User Channel Estimation Results

Here, we first examine the single-user channel estimation scenario. We compare the performance of four distinct KF-based algorithms: standard KF [17], modified KF (Algorithm 1), EKF [25], and NCNKF (Algorithm 2). MSE performance for these algorithms are depicted in Figure 3. From the figure, we can observe that the standard KF exhibits the worst performance because it struggles to handle the non-linear distance-dependent system model. Moreover, our modified KF and EKF exhibit nearly identical performance. Although both algorithms can accommodate non-linearity, they still retain the limitation that they can only handle complex circular noise, which is not a suitable model for the user's movement in this context. The NCNKF algorithm emerges as the most effective because it can handle both the non-linear system model and the non-circular noise.

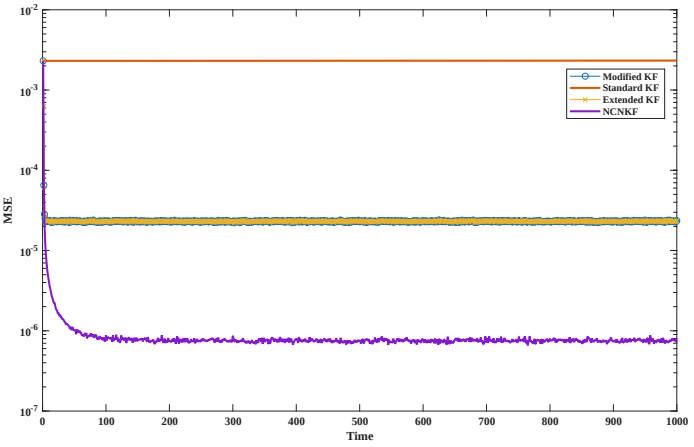

Fig. 3. Channel estimation comparison of different KF-based algorithms

TABLE I
Experiment Parameters Table

Meaning	Symbol	Value
Transmit power	P_{tr}	10
Number of antennas in BS	M	32
Number of elements in RIS	N	16
Length one RIS element	d	0.049 m
Wavelength	λ	0.1
Bandwidth	B	200 kHz
Variance of observation noise	σ_w^2	10^{-6}
Signal-to-noise ratio	SNR	20 dB
Highest speed	α_{max}	300 km/h
Threshold for channel changes	γ	0.1
Time interval	Δt	0.1 ms
Scalar weight of $\boldsymbol{Q}$	q	0.01
Size of 1-D DFT	N_{DFT}	1024
Total number of observation time slots	T	1000

In Figure 4, we compare the MSE in the system with varying numbers of RIS elements N and BS antennas M along the SNR. By adjusting the variance of the observation noise, we observe that the MSE in the system consistently decreases as the SNR increases. Additionally, a higher ratio of $\frac{M}{N}$ results in improved performance. This is because a higher number of BS antennas provides richer spatial diversity and more degrees of freedom for channel estimation. Interestingly, for the same $\frac{M}{N}$ ratio, the performance is remarkably close to each other. However, the system with a lower number of antennas slightly outperforms the system with a higher number of antennas, which is because more elements lead to higher estimation complexity and lower effective SNR per element.

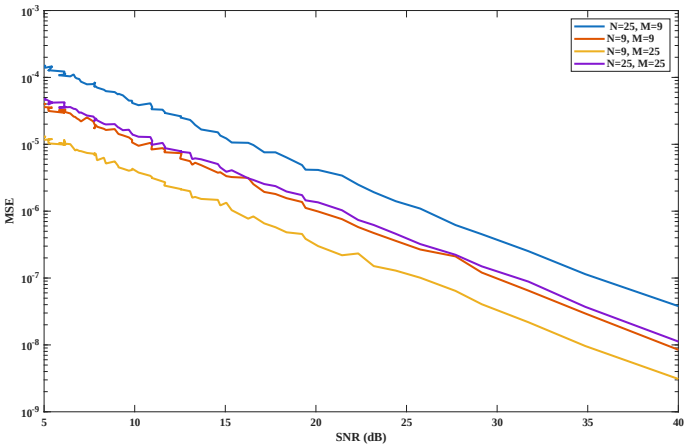

Fig. 4. MSE comparison along SNR for different N, M in case of NCNKF

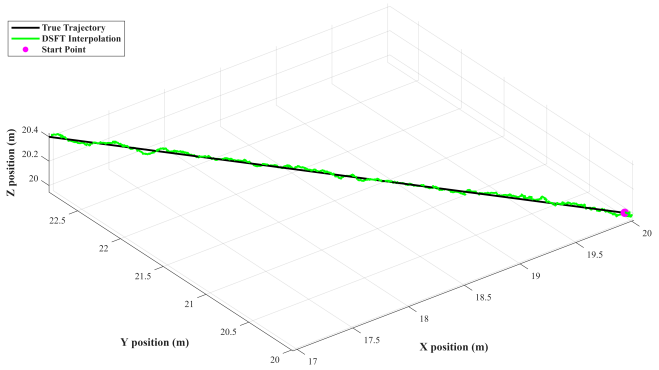

Fig. 5. True and Estimated User Trajectory Comparison

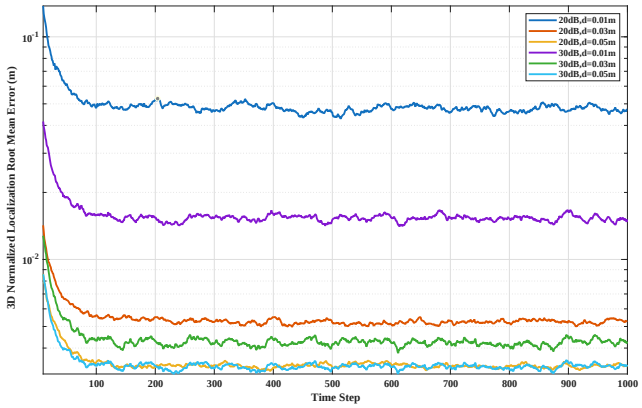

Fig. 6. User Localization Error Comparison for Different Edge Length and SNRs

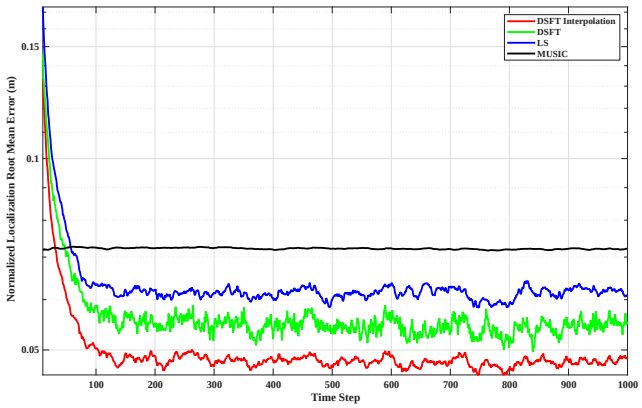

Fig. 7. User Localization Error Comparison for Different Algorithms

B. Single User Localization Results

In this section, we analyze the single-user case with the linear user movement scenario. Algorithm 3 is used to produce estimates of the user's positions. The trajectory of the estimated user positions is depicted in Figure 5. In this figure, the magenta dot represents the user's initial position, the black line denotes its linear trajectory, and the green line represents the estimated user's positions based on the DSFT interpolation method. It is obvious that the estimated user trajectory closely approximates the true movement, demonstrating the effectiveness of the NCNKF-based DSFT interpolation method in handling user localization across various user movement types.

In Figure 6, we compare the user localization error along time for different lengths of the RIS element edge d. The figure shows that as d increases, the localization error decreases. This improvement can be explained by the fact that a larger d enhances the array's angular sensitivity and improves the spatial focusing capability. As expected, a higher SNR generally results in better localization performance due to reduced observation noise. However, the performance gap between different SNRs decreases as d increases. Specifically, when $d = 0.049$ m, the localization errors for 20 dB and 30 dB are almost identical. This happens because the system's localization accuracy is primarily limited in this case by geometric and model-related factors rather than by noise at larger d.

In Figure 7, we compare the normalized RMSE of user localization using various algorithms: the Least Squares (LS) method [39], the Multiple Signal Classification (MUSIC) algorithm [40], DSFT, and the DSFT interpolation method (Algorithm 3). It's worth noting that the LS method has a constraint that $d \leq \frac{\lambda}{2\sqrt{2}(\sqrt{N}-1)}$ to ensure a unique solution. Consequently, we set $d = 0.01$m for all these algorithms. From the figure, we can observe that the DSFT interpolation method achieves the best performance among the algorithms. Although the LS method outperforms MUSIC, as shown in Figure 6, when we increase the value of the element edge length d, all the other three algorithms surpass the LS method significantly.

C. Discussion of Channel Estimation Rate

In this section, we discuss the channel estimation rate for our proposed RIS-aided wireless communication

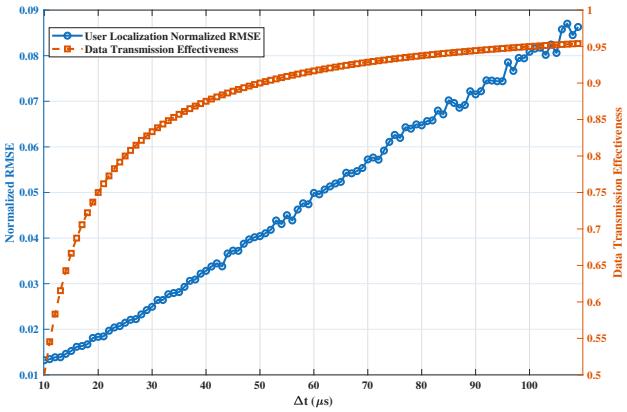

Fig. 8. Normalized RMSE and Data Transmission Effectiveness Comparison along Δt

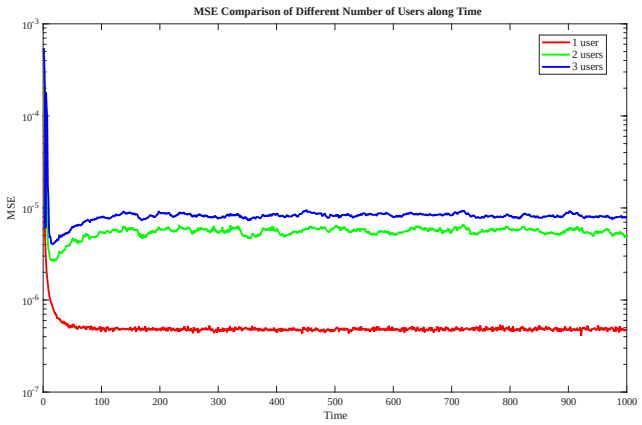

Fig. 9. Channel Estimation Comparison for Different Numbers of Users

system model. Let us assume that each pilot signal occupies a single symbol interval for transmission, and the time required for channel estimation in BS is negligible. Therefore, the effective time available for data transmission is $\Delta t - \frac{1}{B}$. The resulting data transmission effectiveness can be expressed as:

$$\eta = \frac{\Delta t - \frac{1}{B}}{\Delta t} = 1 - \frac{1}{B\Delta t} \tag{52}$$

where η represents the proportion of each time slot Δt allocated to data transmission.

In general, there is an inherent trade-off between the data transmission effectiveness, channel estimation accuracy, and computational complexity. Specifically, a smaller Δt increases the frequency of channel estimation, which typically reduces estimation error but raises computational demands and reduces the time available for data transmission. Conversely, a larger Δt increases the transmission effectiveness but may lead to higher channel estimation errors.

Thus, determining an appropriate time interval Δt is crucial for improving overall system performance. For instance, using values shown in Table I, let us set the wavelength $\lambda = 0.1$, bandwidth $B = 200$ kHz, maximum user speed $\alpha_{max} = 300$ km/h, and $\gamma = 0.1$. Then, according to (35), the feasible time interval is $5\,\mu s \leq \Delta t \leq 148\,\mu s$. Hence, Δt within this range can be selected based on specific system requirements and performance targets.

Figure 8 illustrates the trade-off between the data transmission effectiveness and user localization error. As shown in the figure, increasing Δt results in higher values for both the normalized RMSE and the data transmission effectiveness. This happens since with a fixed pilot transmission time ($\frac{1}{B}$), a longer time slot Δt allows for more data transmission. However, a larger Δt also means a lower channel estimation rate ($\frac{1}{\Delta t}$), so the KF updates less frequently and the user travels longer between updates. This leads to greater errors in both channel estimation and user localization. Notably, while the normalized localization error increases approximately linearly with Δt, the data transmission ratio gradually converges to around 0.96. Therefore, it is generally preferable to select a relatively smaller Δt to achieve better overall system performance.

In practice, Δt can be adjusted according to specific system requirements. For example, if the user moves more slowly, a larger Δt can be chosen to allocate more time for data transmission, as the channel will vary less rapidly. Also, if the system supports a larger bandwidth, a smaller Δt can be used to improve estimation accuracy, taking advantage of the reduced pilot transmission time.

D. Multi-users Channel Estimation and User Localization

In this section, we delve with the multi-user scenario. We present the performance of Algorithm 4 for both channel estimation and user localization, and compare the results for various numbers of users in Figures 9 and 10. From these figures, we observe that as the number of users increases, the error for both channel estimation and user localization also increases. While there are some gaps in the MSE between the single-user and multi-user cases, it appears that the 2-user and 3-user cases exhibit almost similar performance, indicating low sensitivity w.r.t. the number of users.

VII. Conclusion

This paper aims to reduce the MSE of channel estimation and the RMSE of user localization in wireless communication systems with RIS and multiple mobile users. To achieve this, we modify the Kalman Filter and propose the NCNKF algorithms to lower the MSE for distance-dependent channels. Additionally, we apply the DSFT interpolation method to reduce the RMSE for user localization in the case of position-dependent channels. The numerical results and detailed discussions within the paper demonstrate the improvements enabled by our methodology. Several research directions may be further

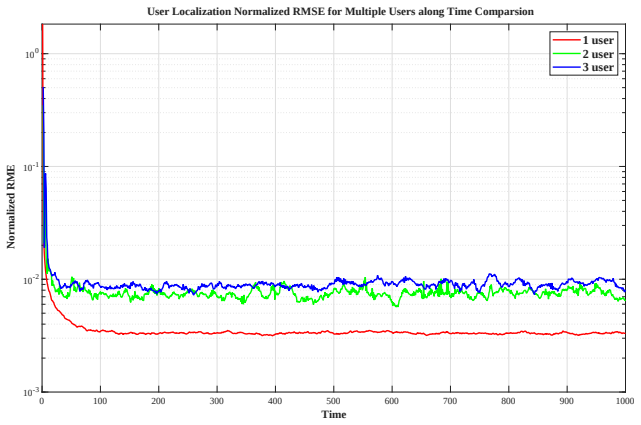

Fig. 10. User Localization Comparison for Different Numbers of Users

considered for the techniques discussed in this paper. E.g., while we use the square RIS with independent phase shift in this paper, exploring other shapes of the RIS and dependent phase shifts could lead to a more flexible system and potentially better performance. Furthermore, investigating the potential of machine learning algorithms to autonomously optimize the RIS phase adjustments based on real-time data could result in more adaptive and responsive communication systems.

References

[1] W. Chen, X. Lin, J. Lee, A. Toskala, S. Sun, C. F. Chiasserini, and L. Liu, "5G-advanced toward 6G: Past, present, and future," IEEE Journal on Selected Areas in Communications, vol. 41, no. 6, pp. 1592–1619, 2023.

[2] M. Banafaa, I. Shayea, J. Din, M. Hadri Azmi, A. Alashbi, Y. Ibrahim Daradkeh, and A. Alhammadi, "6G mobile communication technology: Requirements, targets, applications, challenges, advantages, and opportunities," Alexandria Engineering Journal, vol. 64, pp. 245–274, 2023.

[3] Y. Liu, X. Liu, X. Mu, T. Hou, J. Xu, M. Di Renzo, and N. Al-Dhahir, "Reconfigurable intelligent surfaces: Principles and opportunities," IEEE Communications Surveys & Tutorials, vol. 23, no. 3, pp. 1546–1577, 2021.

[4] W. Tang, M. Z. Chen, X. Chen, J. Y. Dai, Y. Han, M. Di Renzo, Y. Zeng, S. Jin, Q. Cheng, and T. J. Cui, "Wireless communications with reconfigurable intelligent surface: Path loss modeling and experimental measurement," IEEE Transactions on Wireless Communications, vol. 20, no. 1, pp. 421–439, 2021.

[5] M. Najafi, V. Jamali, R. Schober, and H. V. Poor, "Physics-based modeling and scalable optimization of large intelligent reflecting surfaces," IEEE Transactions on Communications, vol. 69, no. 4, pp. 2673–2691, 2021.

[6] S. Kosulnikov, F. S. Cuesta, X. Wang, and S. A. Tretyakov, "Simple link-budget estimation formulas for channels including anomalous reflectors," IEEE Transactions on Antennas and Propagation, vol. 71, no. 6, pp. 5276–5288, 2023.

[7] G. Gradoni and M. Di Renzo, "End-to-end mutual coupling aware communication model for reconfigurable intelligent surfaces: An electromagnetic-compliant approach based on mutual impedances," IEEE Wireless Communications Letters, vol. 10, no. 5, pp. 938–942, 2021.

[8] S. Shen, B. Clerckx, and R. Murch, "Modeling and architecture design of reconfigurable intelligent surfaces using scattering parameter network analysis," IEEE Transactions on Wireless Communications, vol. 21, no. 2, pp. 1229–1243, 2022.

[9] J. Huang, C.-X. Wang, Y. Sun, R. Feng, J. Huang, B. Guo, Z. Zhong, and T. J. Cui, "Reconfigurable intelligent surfaces: Channel characterization and modeling," Proceedings of the IEEE, vol. 110, no. 9, pp. 1290–1311, 2022.

[10] H. Liu, W. K. New, H. Xu, Z. Chu, K.-F. Tong, K.-K. Wong, and Y. Zhang, "Path loss and surface impedance models for surface wave-assisted wireless communication system," IEEE Access, vol. 12, pp. 125 786–125 799, 2024.

[11] L. Hao, F. S. Cuesta, and S. A. Tretyakov, "Comparison of simplistic system-level RIS models and diffraction-theory solutions," in 2024 18th European Conference on Antennas and Propagation (EuCAP), 2024, pp. 1–5.

[12] Y. Liu and C. D. Sarris, "Efficient computation of scattered fields from reconfigurable intelligent surfaces for propagation modeling," IEEE Transactions on Antennas and Propagation, vol. 72, no. 2, pp. 1817–1826, 2024.

[13] C. Pradhan, A. Li, L. Song, B. Vucetic, and Y. Li, "Hybrid precoding design for reconfigurable intelligent surface aided mmWave communication systems," IEEE Wireless Communications Letters, vol. 9, no. 7, pp. 1041–1045, 2020.

[14] S. Li, B. Duo, X. Yuan, Y.-C. Liang, and M. Di Renzo, "Reconfigurable intelligent surface assisted UAV communication: Joint trajectory design and passive beamforming," IEEE Wireless Communications Letters, vol. 9, no. 5, pp. 716–720, 2020.

[15] T. Hou, Y. Liu, Z. Song, X. Sun, Y. Chen, and L. Hanzo, "Reconfigurable intelligent surface aided NOMA networks," IEEE Journal on Selected Areas in Communications, vol. 38, no. 11, pp. 2575–2588, 2020.

[16] G. Singh, A. Srivastava, and V. A. Bohara, "Visible light and reconfigurable intelligent surfaces for beyond 5G V2X communication networks at road intersections," IEEE Transactions on Vehicular Technology, vol. 71, no. 8, pp. 8137–8151, 2022.

[17] Z. Mao, M. Peng, and X. Liu, "Channel estimation for reconfigurable intelligent surface assisted wireless communication systems in mobility scenarios," China Communications, vol. 18, no. 3, pp. 29–38, 2021.

[18] C. Ozturk, M. F. Keskin, V. Sciancalepore, H. Wymeersch, and S. Gezici, "RIS-aided localization under pixel failures," IEEE Transactions on Wireless Communications, vol. 23, no. 8, pp. 8314–8329, 2024.

[19] W. Lyu, S. Yang, Y. Xiu, Y. Li, H. He, C. Yuen, and Z. Zhang, "CRB minimization for RIS-aided mmWave integrated sensing and communications," IEEE Internet of Things Journal, vol. 11, no. 10, pp. 18 381–18 393, 2024.

[20] X. Guo and S. Zhang, "On the secrecy performance of aerial IRS-assisted wireless communications," in MILCOM 2023 - 2023 IEEE Military Communications Conference (MILCOM), 2023, pp. 864–869.

[21] J. An, C. Yuen, C. Huang, M. Debbah, H. Vincent Poor, and L. Hanzo, "A tutorial on holographic MIMO communications—part I: Channel modeling and channel estimation," IEEE Communications Letters, vol. 27, no. 7, pp. 1664–1668, 2023.

[22] C. Skouroumounis and I. Krikidis, "Fluid antenna with linear MMSE channel estimation for large-scale cellular networks," IEEE Transactions on Communications, vol. 71, no. 2, pp. 1112–1125, 2023.

[23] Y. Chen, Y. Wang, Z. Wang, and Z. Han, "Angular-distance based channel estimation for holographic MIMO," IEEE Journal on Selected Areas in Communications, vol. 42, no. 6, pp. 1684–1702, 2024.

[24] K.-Y. Han, S.-W. Lee, J.-S. Lim, and K.-M. Sung, "Channel estimation for OFDM with fast fading channels by modified Kalman filter," IEEE Transactions on Consumer Electronics, vol. 50, no. 2, pp. 443–449, 2004.

[25] L. Chen, S. Zhou, and W. Wang, "MmWave beam tracking with spatial information based on extended Kalman filter," IEEE Wireless Communications Letters, vol. 12, no. 4, pp. 615–619, 2023.

[26] D. Yu, G. Zheng, A. Shojaeifard, S. Lambotharan, and Y. Liu, "Kalman filter based channel tracking for RIS-assisted multi-user networks," IEEE Transactions on Wireless Communications, vol. 23, no. 4, pp. 3856–3869, 2024.

[27] M. Ammous and S. Valaee, "Positioning and tracking using reconfigurable intelligent surfaces and extended Kalman filter," in 2022 IEEE 95th Vehicular Technology Conference: (VTC2022-Spring), 2022, pp. 1–6.
[28] J. Zhang, Z. Zheng, Z. Fei, and Z. Han, "Energy-efficient multiuser localization in the RIS-assisted IoT networks," IEEE Internet of Things Journal, vol. 9, no. 20, pp. 20 651–20 665, 2022.
[29] A. Albanese, P. Mursia, V. Sciancalepore, and X. Costa-Pérez, "PAPIR: Practical RIS-aided localization via statistical user information," in 2021 IEEE 22nd International Workshop on Signal Processing Advances in Wireless Communications (SPAWC), 2021, pp. 531–535.
[30] H. Zhang, H. Zhang, B. Di, K. Bian, Z. Han, and L. Song, "Metalocalization: Reconfigurable intelligent surface aided multi-user wireless indoor localization," IEEE Transactions on Wireless Communications, vol. 20, no. 12, pp. 7743–7757, 2021.
[31] H. Xie and D. Li, "To reflect or not to reflect: On–off control and number configuration for reflecting elements in RIS-aided wireless systems," IEEE Transactions on Communications, vol. 71, no. 12, pp. 7409–7424, 2023.
[32] Z. Ju and M. Doroslovački, "Mobile RIS-channel estimation with Kalman filter and learning," in 2024 58th Asilomar Conference on Signals, Systems, and Computers, 2024, pp. 1570–1574.
[33] S. Sun, R. Li, C. Han, X. Liu, L. Xue, and M. Tao, "How to differentiate between near field and far field: Revisiting the Rayleigh distance," IEEE Communications Magazine, vol. 63, no. 1, pp. 22–28, 2025.
[34] T. Ma, Y. Xiao, X. Lei, W. Xiong, and M. Xiao, "Spreading CDMA via RIS: Multipath separation, estimation, and combination," IEEE Internet of Things Journal, vol. 10, no. 13, pp. 11 396–11 413, 2023.
[35] E. Ollila, J. Eriksson, and V. Koivunen, "Complex elliptically symmetric random variables—generation, characterization, and circularity tests," IEEE Transactions on Signal Processing, vol. 59, no. 1, pp. 58–69, 2011.
[36] Z. Ju and M. Doroslovački, "Mobile user-RIS channel estimation using Kalman filter based approaches," in 2025 59th Annual Conference on Information Sciences and Systems (CISS), 2025, pp. 1–6.
[37] M. Fitton, A. Nix, and M. Beach, "Propagation aspects of frequency hopping spread spectrum," in Proceedings of 8th International Symposium on Personal, Indoor and Mobile Radio Communications - PIMRC '97, vol. 2, 1997, pp. 640–644 vol.2.
[38] I. Alamzadeh, G. C. Alexandropoulos, N. Shlezinger, and M. F. Imani, "A reconfigurable intelligent surface with integrated sensing capability," Scientific reports, vol. 11, no. 1, p. 20737, 2021.
[39] L. Zhao, X. Guo, H. Wu, and J. Ge, "Multi-epoch least-squares joint solution for anchor self-localization: Exemplified with UWB," IEEE Internet of Things Journal, pp. 1–1, 2025.
[40] P. Ramezani, A. Kosasih, and E. Björnson, "An efficient modified MUSIC algorithm for RIS-assisted near-field localization," in GLOBECOM 2024 - 2024 IEEE Global Communications Conference, 2024, pp. 4430–4435.